Received September 14, 2020, accepted September 19, 2020, date of publication September 22, 2020,
date of current version October 1, 2020.

Digital Object Identifier 10.1109/ACCESS.2020.3025946

Performance Analysis of Internal Solitary Wave Detection and Identification Based on Compact Polarimetric SAR

HAO ZHANG[1], JUNMIN MENG[1,2], (Member, IEEE), LINA SUN[1,2], XI ZHANG[1,2], (Member, IEEE), AND SIJING SHU[3]

[1]First Institute of Oceanography, Ministry of Natural Resources of China, Qingdao 266061, China
[2]Ocean Telemetry Technology Innovation Center, Ministry of Natural Resources of China, Qingdao 266061, China
[3]PIESAT Information Technology Company Ltd., Beijing 100195, China

Corresponding author: Junmin Meng (mengjm@fio.org.cn)

This work was supported in part by the National Key Research and Development Program of China under Grant 2016YFA0600102; and in part by the Special Project for Global Change and Air-sea Interaction of Ministry of Natural Resources, China, under Grant GASI-02-IND-YGST2-04, Grant GASI-02-SCS-YGST2-04, and Grant GASI-02-PAC-YGST2-04.

ABSTRACT This paper studies the application of compact polarimetric (CP) SAR in the detection and identification of ocean internal solitary waves (ISWs). First, based on full-polarimetric ALOS PALSAR images, we construct CP SAR images and extract 26 CP features. Then, the ISWS-sea surface differentiation capability for the different polarization features is analyzed by using the Jeffries and Euclidean distances. The results show that λ_1, Entropy (H), *Lambda*, the polarimetric total power (*Span*) and the Stokes parameters ($Stokesg_0$, and $Stokesg_3$) improve the ISWs detection results. On this basis, a *k-means* clustering algorithm based on CP features is introduced, and the results show that the ISWs detection and identification performance of the algorithm are superior to that of the traditional *Wishart* polarization clustering algorithm, which suggests that CP SAR has good application prospects in the detection and identification of ocean ISWs.

INDEX TERMS Internal solitary waves, compact polarimetric SAR, detection, polarization features.

I. INTRODUCTION

Internal solitary waves (ISWs) in the ocean refer to waves generated in a stable density stratification, and the maximum amplitude appears within the ocean [1]. Its crest length can reach several hundred kilometers, and the period is generally several minutes to dozens of hours. At present, the measured maximum amplitude of ISWs is approximately 240 m [2]. ISWs play an important role in energy transfer and material transport in the ocean and pose a great threat to marine engineering structures and military operations [1]. Therefore, it is very important to study the detection and identification of ISWs to reduce or avoid the loss of resources, impacts on fishing and commercial shipping and other issues caused by ISWs.

ISWs detection has always been of great concern to marine scientists. In situ direct observation is the best way to study ISWs, but this approach is expensive, and large-scale information is difficult to obtain. With the development of remote sensing technology, visible spectral, altimeter and synthetic aperture radar (SAR) sensors have gradually become the main tools used in the observation of ISWs. In particular, SAR in the microwave band has the advantages of all-weather use and high-resolution imaging [3], and has thus accelerated studies of ISWs. For example, in [4], Liu *et al* used European Remote Sensing (ERS) -1 SAR images to study the evolution of ISWs in the East China Sea and the South China Sea. In [5], Zhao *et al* based on ERS-2 SAR images of ISWs with large amplitudes, proposed that ISWs with large amplitudes are not generated by the Lee mechanism but by the nonlinear steepening principle of baroclinic tides. In [6], Azevedo *et al* studied the generation and propagation of ISWs in the Bay of Biscay using ERS SAR and Envisat SAR images and identified the local generation mechanism of ISWs in combination with ray theory and body forces. In [7], Zheng *et al* used SAR images from 1995 to 2001 to analyze the spatial and temporal distribution characteristics of ISWs in the South China Sea. In [8], using ERS-1/2, Envisat-1, and Sentinel-1A/B SAR images, Wang *et al* obtained over 500 sets of internal wave packets, discussed the spatial and temporal

The associate editor coordinating the review of this manuscript and approving it for publication was Weimin Huang.

distribution characteristics of ISWs in the Georgia Strait, and analyzed the relationships between ISWs and tidal and wind fields. In [9], Pisoni *et al* used Advanced Land Observing Satellite (ALOS) Phase Array type L-band SAR (PALSAR) images to study ISWs on the Argentine inner Patagonian shelf and evaluated their generation mechanism and propagation speed. In [10], Nadimpalli *et al* used Envisat and TerraSAR-X images to study the potential generation locations of ISWs in the Andaman Sea.

The SAR imaging mechanisms of ISWs mainly consist of three complex physical processes [11]. These physical processes cause ISWs to produce special electromagnetic scattering characteristics at the ocean surface, which in turn cause peaks and troughs to appear as alternating bright and dark bands in SAR images [12]. However, polarimetric SAR has sensitive electromagnetic wave response characteristics [13], so it can be used to detect and characterize targets with abundant polarimetric information, such as ISWs.

SAR systems have developed from single-polarization to dual-polarization (DP) and even full-polarization (FP) observation modes. Compared with single-polarization SAR, FP SAR can completely describe the vector relationship between an incident wave and the scattered wave of the target, and the acquired target information is abundant. In [14], Schuler *et al* first applied FP SAR for ISWs detection, and studied the influence of ISWs fronts on the polarization orientation angle, thus providing a new way to identify these marine features. In [15], based on FP SAR images, Li *et al* comparatively analyzed the visibility of ISWs in 11 polarization feature images. However, due to the narrow width of FP SAR images (for example, the width of an FP RADARSAT-2 SAR image is only 25-50 km), such images cannot meet the requirements of large-scale ISWs survey applications.

To solve the problem of FP SAR systems, Souyris and Mingot proposed the concept of compact polarimetric (CP) SAR [16]. Compared with FP SAR, CP SAR can not only reduce the design complexity and improve the coverage width of the image but also maintain the polarization capability of an FP SAR system to a certain extent [17]. Preliminary studies, such as that of Shirvany *et al*, who detected ships on the sea surface based on the polarization degree extracted from CP SAR, have been conducted in the field of target detection [18]. In [19], Cao *et al* constructed CP SAR data based on FP RADARSAT-2 data and compared the ship detection capabilities of FP, CP and DP SAR systems. In [20], Salberg *et al* introduced some CP features for the detection of oil spills; additionally, the polarization degree and ellipticity, which were obtained from $\lambda - m$ decomposition, were used for oil spill detection. However, in the field of ISWs, research using CP SAR technology for detection is still lacking.

Considering the above problems, this paper uses FP ALOS PALSAR images to construct CP images. Then, we extract some features through polarization decomposition and other processing steps and analyze the ISWs detection and identification characteristics of these features in detail. We discuss the feasibility of using CP SAR technology for ISWs detection and identification and for the selection of polarization features that can be effectively used for ISWs detection. This work improves the general scientific understanding of ISWs and provides a reference for follow-up work on the detection and automatic extraction of SAR ISWs.

TABLE 1. The specific information of the 5 SAR images.

Image Number	Image Name	Imaging Area	Incidence Angle
#1	ALPSRP065000120	Andaman Sea	23.93°
#2	ALPSRP233480140	Andaman Sea	25.73°
#3	ALPSRP274470120	Andaman Sea	23.95°
#4	ALPSRP229970140	Sulu Sea	25.73°
#5	ALPSRP229970180	Sulu Sea	25.72°

II. DATA

A. DATA INTRODUCTION

In this paper, FP ALOS PALSAR SAR images are used. PALSAR is an L-band SAR sensor carried by the Japanese ALOS-1 satellite. The Level 1.1 products provided by PALSAR are all complex single-look data sets. The images have undergone azimuth and range compression, with an azimuth resolution of approximately 24 m and a range resolution of approximately 10 m. In total, 145 scenes of ALOS PALSAR Level 1.1 images are selected to perform the research presented in this paper. Five scenes were selected to screen the features for compact polarization. These images were acquired in the Andaman Sea and the Sulu Sea because the ISWs in these two areas have obvious characteristics, with large amplitude and spatial scale. Another 140 scenes were used for subsequent ISWs classification and identification analysis, and they were obtained from different ocean regions of the world, such as the South China Sea and the waters near Colón Island.

Figure 1 shows the Pauli-based pseudocolor composite images (PauliRGB) of the above 5 scenes. The ISWs in images #1-3 propagate in the range direction, and the ISWs in images #4-5 propagate in the azimuth direction.

B. DATA PROCESSING

The CP SAR system considered in this paper is essentially a special DP SAR system. Due to the lack of real CP data, most studies use FP images reconstruction to generate CP images. In this paper, CP SAR images are also constructed based on ALOS PALSAR images. Since the original FP images include single-look complex data and the images are narrow and long, ISWs information is difficult to obtain. Therefore, during data processing, the original SAR data are first processed with a multilook method in the azimuth direction, and the number of looks is 6. Then, the FP images are filtered after multilook processing because the single-frequency electromagnetic wave emitted by the SAR system is scattered by distributed ground objects, the echoes of different scattering surface elements contain wave path differences, and the coherent superposition of echoes generates coherent

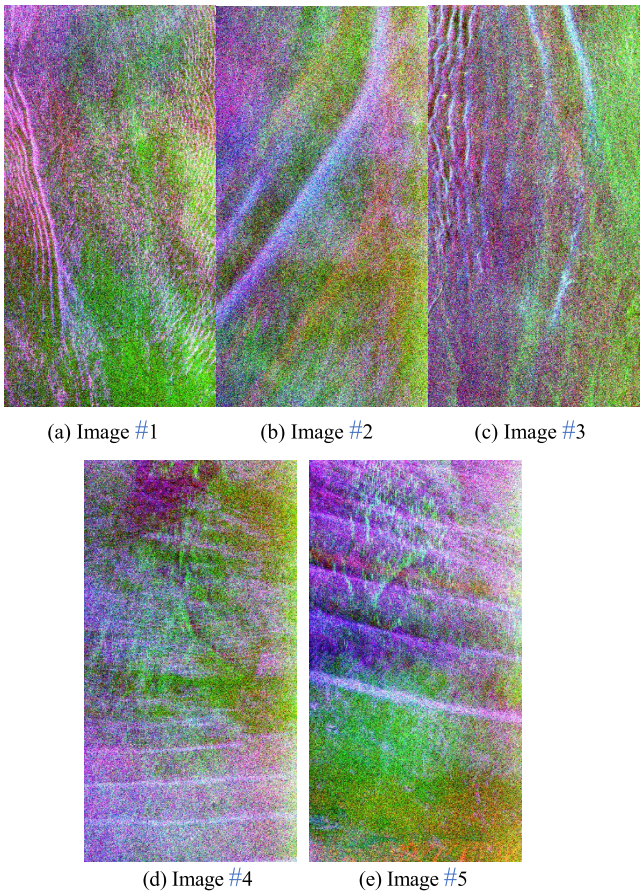

(a) Image #1 (b) Image #2 (c) Image #3

(d) Image #4 (e) Image #5

FIGURE 1. 5 ALOS PALSAR PauliRGB images.

speckles, which increase the difficulty in interpreting polarized SAR images and affect the detection, identification and classification of targets [21]. In scientific research, a specific filtering algorithm is often used to remove speckle noise in original SAR images, and the Refined Lee filtering algorithm is used in this paper [21]. Finally, based on the filtered FP SAR images, CP SAR images are constructed. Then, polarization decomposition and other processing methods are used to extract CP features, and these feature images are used for the detection and identification of ocean ISWs.

III. COMPACT POLARIZATION FEATURES

A. FEATURE EXTRACTION

Compared with the FP SAR system, the CP SAR system emits electromagnetic waves only in one direction, and the waves are generally linear polarization waves or circular polarization waves of 45°. However, the echo signals from both directions are received at the same time, namely, as horizontal and vertical echoes or circularly polarized waves. At present, there are three main modes of CP SAR: $\pi/4$, circular-to-circular (CC) and hybrid-polarity (HP) modes. In this paper, we choose the HP mode. This mode uses right-hand circular polarization transmission and horizontal and vertical linear polarization reception methods to reconstruct fully polarimetric information [22]. The polarization scattering vector is expressed as follows:

$$\begin{aligned}\vec{k} &= \begin{bmatrix} E_{HC} \\ E_{VC} \end{bmatrix} = \frac{1}{\sqrt{2}} \begin{bmatrix} S_{HH} & S_{HV} \\ S_{VH} & S_{VV} \end{bmatrix} \begin{bmatrix} 1 \\ \pm i \end{bmatrix} \\ &= \frac{1}{\sqrt{2}} \begin{bmatrix} S_{HH} \pm S_{HV} \\ S_{VH} \pm S_{VV} \end{bmatrix} \end{aligned} \tag{1}$$

In the above formula, the subscript 'C' indicates circular polarization, and '+' and '-' represent right-hand and left-hand circular polarization, respectively. 'H' and 'V' indicate horizontal and vertical polarization, respectively. From (1), the covariance matrix of CP SAR is expressed as:

$$C_2 = \left\langle \vec{k}\vec{k}^{*T} \right\rangle = \begin{bmatrix} C_{11} & C_{12} \\ C_{21} & C_{22} \end{bmatrix} = \begin{bmatrix} \langle |S_{RH}|^2 \rangle & \langle S_{RH} S_{RV}^* \rangle \\ \langle S_{RV} S_{RH}^* \rangle & \langle |S_{RV}|^2 \rangle \end{bmatrix}, \tag{2}$$

where 'R' denotes right circular polarization, 'T' is a matrix transpose operation, '*' denotes the complex conjugate, and $<>$ is the spatial average.

The polarization features commonly used for target detection in SAR images can generally be divided into two categories: one category is based on the information obtained from the original SAR data, such as the elements of the polarization coherence matrix or their linear combinations, and the other category is the information obtained through various polarization decompositions. Such information includes polarization entropy and average scattering angle information. Table 2 lists all the polarization features used in this article, which includes 26 CP features and σ_0 images of 4 different polarization channels. Among these features, f_1 and f_2 correspond to the amplitudes of C_{11} and C_{22}, respectively, in (2) [23], and f_3 represents the total polarization power (*Span*) [24], which is expressed as:

$$Span = |S_{RH}|^2 + |S_{RV}|^2 \tag{3}$$

Similar to the theory of fully polarized $HA\alpha$ decomposition, in 2012, Cloude *et al* proposed a compact polarized $HA\alpha$ decomposition method based on the covariance matrix C_2 [23]. This decomposition can obtain the eigenvalues λ_i of the covariance matrix, and the eigenvalues satisfy $\lambda_1 \geq \lambda_2 (f_4 - f_5)$. Using λ_i, a series of features can be obtained, such as the compact polarization entropy (H, f_6), anisotropy (A, f_7) and average scattering angle (α, f_8) [23], [24]. In addition, feature f_9 is the *Lambda* value, which characterizes the ability of the sea surface to reflect electromagnetic waves [13].

In addition to the scattering vector k_p, CP SAR can also be expressed by Stokes vectors [24]:

$$g_{HP} = \begin{bmatrix} g_0 \\ g_1 \\ g_2 \\ g_3 \end{bmatrix} = \begin{bmatrix} \langle |S_{RH}|^2 + |S_{RV}|^2 \rangle \\ \langle |S_{RH}|^2 - |S_{RV}|^2 \rangle \\ 2\mathrm{Im} \langle S_{RH} S_{RV}^* \rangle \\ -2\mathrm{Re} \langle S_{RH} S_{RV}^* \rangle \end{bmatrix} \tag{4}$$

The features $Stokesg_i$ are Stokes vectors $(f_{10} - f_{13})$ [25], where g_0 represents the total power of an electromagnetic

TABLE 2. The compact polarimetric features used in this paper.

Number	Polarization Features
$f_1 - f_2$	$\lvert C_{11}\rvert, \lvert C_{22}\rvert$
f_3	$span$
$f_4 - f_5$	λ_1, λ_2
$f_6 - f_8$	$Entropy(H), Anistropy(A), Alpha(\alpha)$
f_9	$Lambda$
$f_{10} - f_{13}$	$Stokesg_0, Stokesg_1, Stokesg_2, Stokesg_3$
$f_{14} - f_{17}$	$LPR, CPR, DoLP, DoCP$
f_{18}	$Ellipticity\ Angle(tau)$
f_{19}	$Orientation\ Angle(phi)$
f_{20}	$Contrast(con)$
$f_{21} - f_{23}$	χ, m, δ
$f_{24} - f_{26}$	Odd, Dbl, Vol
$f_{27} - f_{30}$	$\sigma_0^{HH}, \sigma_0^{VV}, \sigma_0^{HV}, \sigma_0^{VH}$

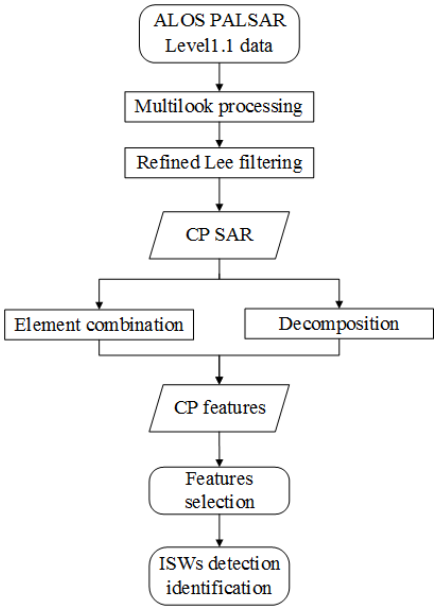

FIGURE 2. Flowchart of the data processing step.

wave, g_1 represents the horizontal or vertical linear polarization component power, g_2 represents the value of linear polarization component power at 45° or 135°, and g_3 is the circularly polarized component power. Based on Stokes vectors, we further obtain the features $f_{14} - f_{20}$, which are the linear polarization ratio and circular polarization ratio (LPR, f_{14}; CPR, f_{15}), the degree of linear polarization and degree of circular polarization ($DoLP, f_{16}$; $DoCP, f_{17}$), the ellipticity Angle (tau, f_{18}), the orientation angle (phi, f_{19}) and the contrast (Con, f_{20}) [25].

Features $f_{21} - f_{23}$ are the roundness (χ, f_{21}), the degree of polarization (m, f_{22}) and the relative phase (δ, f_{23}) extracted from Raney' decomposition, respectively [25]. The corresponding formulas are:

$$m = \frac{\sqrt{g_1^2 + g_2^2 + g_3^2}}{g_0}, \quad \delta = -\tan\left(\frac{g_3}{g_2}\right), \quad \sin 2\chi = \frac{-g_3}{mg_0} \tag{5}$$

The polarization features $f_{24} - f_{26}$ characterize the ability to of the SAR system to detect surface scattering (Odd, f_{24}), double scattering (Dbl, f_{25}) and volume scattering (Vol, f_{26}) of objects.

Finally, $f_{27} - f_{30}$ represent σ_0 images of the copolarization and cross-polarization, respectively.

B. FEATURE SELECTION

The features extracted above have a certain ocean background and ISWs target discrimination ability, but because of their different physical characteristics, their "sensitivity" to ISWs varies. In this paper, based on the differences between the scattering characteristics of ISWs areas and clear sea surface areas, ISWs and sea clutter samples are selected. Then, two detection indexes, the Jeffries distance [26] and Euclidean distance [19], are constructed to evaluate the ISW-sea surface discrimination ability of SAR images for different polarization features. Finally, the CP features that yield the best detection performance for ISWs are selected. To ensure the accuracy of the samples and avoid misjudgments as much as possible, we choose the pixels with the most obvious ISWs characteristics as ISWs samples and clear uniform seawater pixels as sea surface samples. It should be noted that when select ISWs samples, we mainly choose the pixels of the leading wave in the wave packet. The pixels that are spatially scattered and from different regions are selected at the largest possible distances to make the results representative. The 5 images shown in Fig. 1 were used for feature selection, and each image yielded an average of approximately 93,000 ISWs and sea surface pixels. The statistical ISWs and sea surface pixels are marked with red and blue boxes, respectively, in Fig. 6a.

The Jeffries distance and the Euclidean distance between ISWs and the sea surface are defined as:

$$J = \frac{1}{8}(M_{IW} - M_{sea})^2 \frac{2}{\sigma_{IW}^2 + \sigma_{sea}^2} + \frac{1}{2}\ln\frac{\sigma_{IW}^2 + \sigma_{sea}^2}{2\sigma_{IW}\sigma_{sea}} \tag{6}$$

$$D = \frac{|M_{IW} - M_{sea}|}{\sqrt{\sigma_{IW}^2 + \sigma_{sea}^2}} \tag{7}$$

In the above formulas, M_{IW} and M_{sea} represent the mean value of the ISWs and sea surface statistical samples, respectively;σ_{IW}^2 and σ_{sea}^2 represent the variance of the ISWs and sea surface statistical samples, respectively. In the formulas, the two detection indexes are dimensionless because the means and variances of the samples are considered. When J and D are large, ISWs are generally easily distinguishable from the sea surface.

Figure 3 shows the calculation results for the ISWs-sea surface Jeffries distances of the 5 images used in this paper.

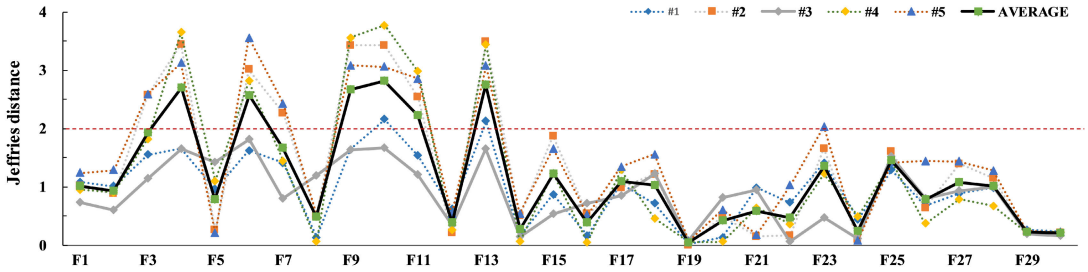

FIGURE 3. Internal solitary waves - sea surface *Jeffries distance* for compact polarization features.

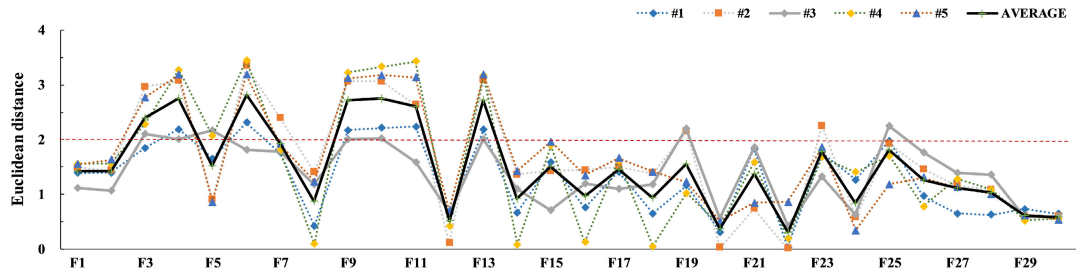

FIGURE 4. Internal solitary waves - sea surface *Euclidean distance* for compact polarization features.

TABLE 3. Internal solitary wave detection capability of compact polarization Features.

Level	Features
I	λ_1, $Entropy(H)$, $Lambda$, $Stokesg_0$, $Stokesg_1$, $Stokesg_3$, $Span$
II	$A, m, \lvert C_{11}\rvert, \lvert C_{22}\rvert, DoCP, \lambda_2, \sigma_0^{HH}, \sigma_0^{VV}, Dbl, Vol, CPR$
III	$Con, \chi, tau, DoLP, \alpha, LPR, Odd, Stokesg_2, \sigma_0^{HV}, \sigma_0^{VH}, phi, \delta$

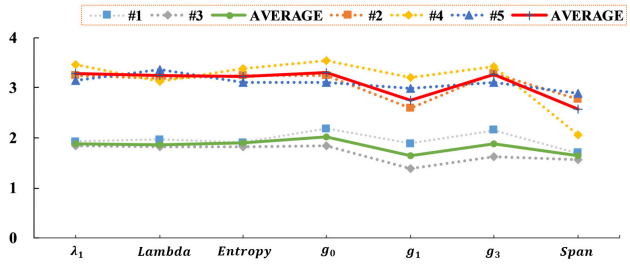

FIGURE 5. Influence of the incident angle on the polarization features.

The solid black line represents the average value. According to the statistical results, the evaluation index J has the same trend for the 5 images, and the only difference is related to the size of the relative value. From the average result, we can see that the Jeffries distances of $Stokesg_0$, $Stokesg_3$, λ_1, $Lambda$, $Entropy$ (H), and $Stokesg_1$ are high, and the ISWs discrimination effect in these images is better than the original images. The Jeffries distances of other features are all less than 2, and their ISWs detection performance is relatively poor.

Similar to the Jeffries distance, the Euclidean distance can reflect the difference between ISWs and the uniform sea surface scattering intensity, and can be used as a measure of the detectability of ISWs. Figure 4 shows the ISWs-sea surface Euclidean distances. In general, the detection results are consistent with those of the Jeffries distance, but unlike in the previous case, the *Span* feature also displays good ISWs-sea surface background discrimination ability.

A comprehensive analysis of the Euclidean distance and Jeffries distance results was performed. Table 3 summarizes the ISWs detection capabilities of the features used in this paper. Notably, the average value of features in Level I is greater than 2 ($(J+D)/2>2$), meaning that these features yield excellent performance in ISWs detection and identification. The average value of features in Level II is between 1 and 2, and the ISWs recognition ability based on these features is relatively poor. The features in Level III represent unrecognizable ISWs, and the average values of the Euclidean distance and Jeffries distance are less than 1. In addition, we should note that the original copolarization σ_0 images and cross-polarization σ_0 images are in Level II and Level III, respectively.

In Table 1, we have listed the specific information of 5 scene images, and we can find that images #1 and #3 have relatively close incident angles of 23.93°, while images #2, #4 and #5 have the same incident angle, that is, 25.72°. To analyze the influence of the radar incidence angle on the selection of polarization features, this paper displays 7 features in Level I. As shown in Fig. 5, the ordinate represents the average Jeffries distance and Euclidean distance. The dashed lines represent the result values of the 5 scene images, and the solid green line represents the average value of images

#1 and #3, whose incident angles are small; the solid red line represents the average of 3 scenes with larger incident angles. It can be seen from the figure that the incidence angle increases, the distance value increases in the different polarization feature images, that is, the distinguishability between ISWs and the sea surface increases. This finding is consistent with the ship detection results by CP features indicated in [27]. However, for images with the same incidence angle, the distance value does not change much, and the overall trend is relatively stable, as shown by the solid line in the figure. The above analysis shows that the incident angle has a reference role in the selection of the polarization features but does not play a decisive role, because for each scene image, the incident angle is fixed. Under this condition, the CP features selected in this paper are better than the ISWs detection performance of the original σ_0 images.

Figure 6 shows seven features in image #3, all of which are categorized as Level I. Compared with the results based on the original PauliRGB images, the visual interpretation results for the ISWs of most of the features in the images are improved, and the features of the ISWs region are highlighted. However, in the $Stokesg_1$ image, the ISWs features are fuzzy and cannot be effectively recognized, as will be verified and explained in the following section. In addition, it should be mentioned that in the feature images shown in Fig. 6, λ_1, *Entropy(H)* and *Lambda* have no units, because they are linear indexes. The remaining 4 features are all displayed in dB, and the pixel values in the $Stokesg_1$ and $Stokesg_3$ images need to be logarithmically converted to achieve dB as the unit.

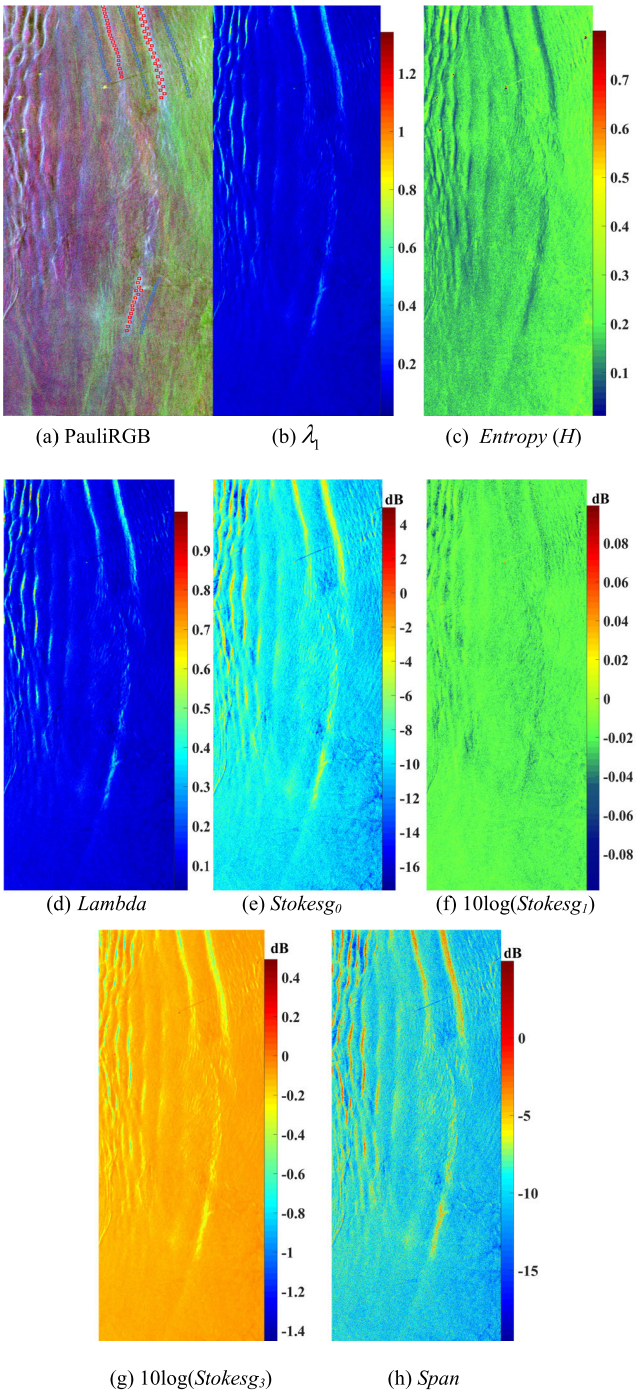

FIGURE 6. Compact polarimetric features of image #3.

IV. CLASSIFICATION

To identify ISWs in remote sensing images, ISWs and the sea background are classified. Based on this principle, the CP features selected above are used as the basis for establishing a simple unsupervised classification method to further study the potential of using such features to detect and identify ISWs at the sea surface. We mainly use the *k-means* clustering algorithm based on the features selected above and the traditional *Wishart* clustering algorithm. The *Wishart* clustering algorithm based on the polarimetric covariance matrix C_2 is regarded as the standard clustering method for processing polarimetric data [28], [29]. When using CP features for *k-means* classification, the features are first logarithmically transformed to enhance the contrast of the data and thus improve the performance of the *k-means* clustering algorithm [29]. Additionally, in *k-means* classification, the number of classes (k) must be determined in advance. In the two cases used in this section, we set the number of classes to 2; that is, only the target type and the sea background type are considered.

A. PERFORMANCE ANALYSIS

To analyze the ISWs identification performance of the above two clustering algorithms, the ISWs identification accuracy of each approach is analyzed, and the results are compared. However, there is no accurate and feasible standard for evaluating the accuracy of ISWs detection in remote sensing images. Therefore, when we evaluate the accuracy of ISWs identification, the standard this paper used is the number of ISWs detected. First, the ISWs were manually identified in the original PauliRGB images and the leading waves were marked with a solid red line in the figure (seen in Fig. 7). Then, the *k-means* clustering algorithm and the *Wishart* algorithm are used to classify the polarization feature images and

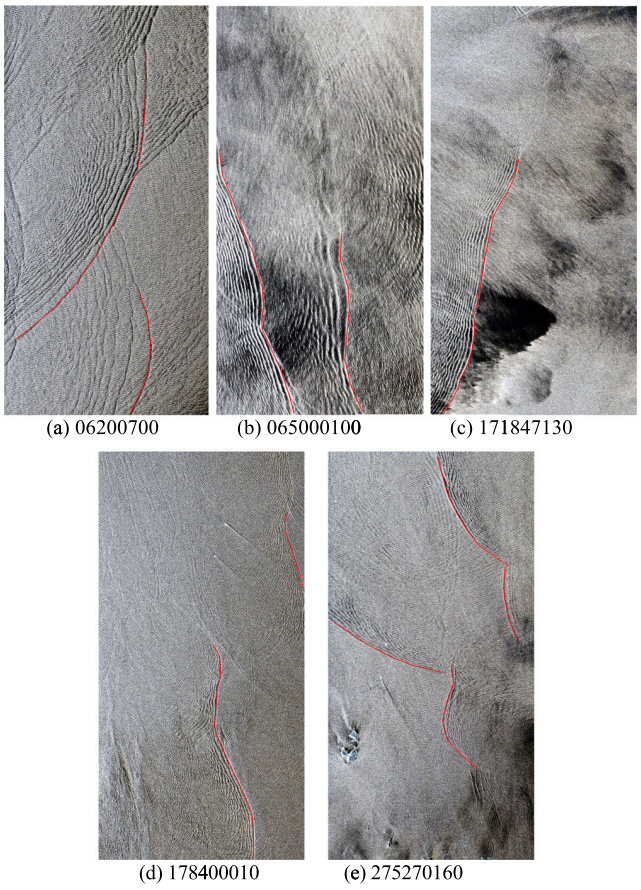

FIGURE 7. For internal solitary wave images, the image name is 'ALPSRP-'. The visual interpretation results of the internal solitary waves in the figure are marked with solid red lines.

the C_2 matrix, respectively, and the classification result is obtained (the ISWs pixels are equal to 1, and the sea pixels are equal to 0). Finally, the artificially marked ISWs areas in the original image were compared pixel by pixel with the corresponding ISWs areas in the classification results. If the pixel coincidence rate reaches 70%, that is, at least 70% of the pixels in the artificially marked area are consistent with the ISWs area detected in the feature images, then the ISWs detection is considered successful.

In this paper, 140 fully polarized ALOS PALSAR images were selected, and 250 ISWs were identified from the images. It should be noted that because ISWs are large-scale marine features, they appear as light and dark bands in the form of wave packets in remote sensing images. Therefore, in this paper, when the ISWs are calibrated, the large connected area at the front of waves is the main area selected.

Table 4 shows that the *Wishart* clustering method is able to identify 194 ISWs with a recognition accuracy of 77.6%. However, the *k-means* clustering algorithm based on compact polarization features yields an excellent ISWs identification performance. λ_1, *Lambda*, *Entropy*(H) and *Span* of ISWs identification are greater than 80%. The ISWs identification accuracies for the $Stokesg_0$ and $Stokesg_3$ features are close to

TABLE 4. Internal solitary wave identification accuracy.

Method	Number	Accuracy
Wishart	194	77.6%
k-means clustering of λ_1	205	82%
k-means clustering of *Lambda*	203	81.2%
k-means clustering of Entropy(H)	207	82.8%
k-means clustering of $Stokesg_0$	192	77%
k-means clustering of $Stokesg_1$	142	57%
k-means clustering of $Stokesg_3$	197	79%
k-means clustering of *Span*	203	81.2%

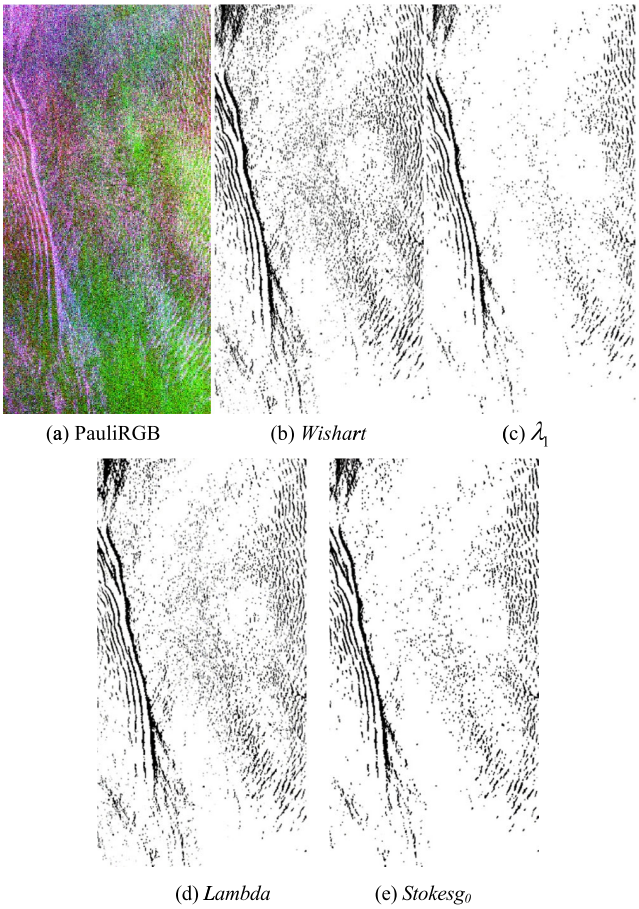

FIGURE 8. Comparison of internal solitary wave clustering results. (a) PauliRGB image (b) *Wishart* clustering results (c) *k-means* clustering results of λ_1 (d) *k-means* clustering results of *Lambda* (e) *k-means* clustering results of $Stokesg_0$.

those obtained with the *Wishart* algorithm at 77% and 79%, respectively. However, only 142 ISWs can be identified in the image of $Stokesg_1$ feature, with a detection accuracy of 57%, suggesting that the ISWs identification ability is poor; therefore, this feature is not suitable for the detection of ocean ISWs. In summary, the partial CP features selected based on the Euclidean distance and Jeffries distance in this paper can be effectively used for the detection and identification of

ocean ISWs, and such features include λ_1, *Lambda*, *Entropy* (H), $Stokesg_0$, $Stokesg_3$ and *Span*.

B. SAMPLE FINDINGS

Figure 8 shows the results of the two clustering algorithms on the ISWs in image #1. This section mainly analyzes three features, namely, λ_1, *Lambda*, and $Stokesg_0$ in Level I. In both images, the targets (ISWs) are shown in black, and the sea background is shown in white. Figure 8 indicates that with both classification methods, the ISWs can be easily distinguished from the background environment, but there is a certain difference between the results of the *Wishart* clustering algorithm and those of the feature-based clustering algorithm. Notably, the *k-means* clustering algorithm based on CP features can highlight the characteristics of the ISWs regions, has a significant denoising effect and effectively maintains the edge features of the ISWs. Thus, the ISWs detection and recognition effects are more accurate than those of the standard *Wishart* classification algorithm. This finding supports the conclusion that the CP features selected in this paper can be used to effectively distinguish ISWs and the ocean background. Although these features do not contain complete polarization information, they contain sufficient information for the purpose of this study.

V. CONCLUSION

CP SAR is an emerging polarization mode that can not only achieve wide swath observations but also fully retain the polarization information of a detected target; therefore, this approach has great potential in the observation and analysis of large-scale marine phenomena. However, in the field of CP SAR, current research on the detection of ocean ISWs is still lacking, and the use of CP SAR technology for the detection and identification of ocean ISWs has become an increasingly popular issue. Therefore, this paper focuses on the detection and identification of marine ISWs with spaceborne CP SAR.

In this paper, based on the reconstruction of FP ALOS PALSAR images, CP SAR data in HP mode are obtained. On the basis of the proposed extraction method for CP features, the ISWs and sea background discrimination abilities obtained with different polarization features are systematically analyzed based on the Jeffries distance and Euclidean distance. The results show that some CP features can be effectively used for ISWs detection and identification research, such as λ_1, *Lambda*, *Entropy* (H), $Stokesg_0$, $Stokesg_3$ and *Span*, and their ISWs detection capabilities exceed the original copolarization and cross-polarization σ_0 images.

By using the selected features as the basis of simple unsupervised classification, the *k-means* clustering algorithm proposed in this paper outperforms the traditional *Wishart* polarization clustering algorithm and has advantages in the identification of ISWs and the determination of the characteristics of ISWs regions. Combined with an accuracy evaluation based on expert interpretation, the results show that the accuracy of the *Wishart* clustering algorithm in ISWs identification is 77.6%, and λ_1, *Lambda*, *Entropy* (H) and *Span* yield accuracies greater than 80% in ISWs identification. The identification accuracies of $Stokesg_0$ and $Stokesg_3$ are close to those achieved by the *Wishart* algorithm at 77% and 79% respectively. In other words, these features contain sufficient information to detect and identify ISWs.

This paper explores the potential of ISWs detection using CP SAR technology. The polarization scattering characteristics of ISWs are beyond the scope of this article and require further research to improve the overall understanding of ISWs and promote the automatic detection and extraction of ISWs in SAR images.

ACKNOWLEDGMENT

The authors thank the Japan Aerospace Exploration Agency (JAXA) for providing the ALOS PALSAR data and the European Space Agency (ESA) for providing the Polarimetric SAR data Processing and Education Toolbox (PolSARpro).

REFERENCES

[1] S. Z. S. Feng, F. Q. Li, and S. J. Li, *An Introduction to Marine Science*. Beijing, China: Higher Education Press, 1999, pp. 190–195.

[2] A. N. Rutenko, "The effect of internal waves on the sound propagation in the shelf zone of the Sea of Japan in different seasons," *Acoust. Phys.*, vol. 51, no. 4, pp. 449–456, Aug. 2005, doi: 10.1134/1.1983608.

[3] H. Lin, K. G. Fan, H. Shen, W. G. Huang, and M. X. He, "Review on remote sensing of oceanic internal wave by space-borne SAR," *Prog. Geophys.*, vol. 25, no. 3, pp. 1081–1091, Jun. 2010, doi: 10.3788/HPLPB20102209.2186.

[4] A. K. Liu, Y. S. Chang, M.-K. Hsu, and N. K. Liang, "Evolution of nonlinear internal waves in the east and south China seas," *J. Geophys. Res., Oceans*, vol. 103, no. C4, pp. 7995–8008, Apr. 1998, doi: 10.1029/97JC01918.

[5] Z. X. Zhao, V. Klemas, Q. A. Zheng, and X. H. Yan, "Remote sensing evidence for baroclinic tide origin of internal solitary waves in the northeastern South China Sea," *Geophys. Res. Lett.*, vol. 31, no. 6, pp. 302–306, Mar. 2004, doi: 10.1029/2003GL019077.

[6] A. Azevedo, J. C. B. da Silva, and A. L. New, "On the generation and propagation of internal solitary waves in the southern bay of biscay," *Deep Sea Res. I, Oceanographic Res. Papers*, vol. 53, no. 6, pp. 927–941, Jun. 2006, doi: 10.1016/j.dsr.2006.01.013.

[7] Q. Zheng, R. D. Susanto, C.-R. Ho, Y. T. Song, and Q. Xu, "Statistical and dynamical analyses of generation mechanisms of solitary internal waves in the northern south China sea," *J. Geophys. Res.*, vol. 112, no. C3, pp. 21–37, Mar. 2007, doi: 10.1029/2006JC003551.

[8] C. X. Wang, X. Wang, and J. C. B. da Silva, "Studies of internal waves in the strait of Georgia based on remote sensing images," *Remote Sens.*, vol. 11, no. 1, pp. 96–112, Jan. 2019, doi: 10.3390/rs11010096.

[9] J. P. Pisoni, N. G. Glembocki, S. I. Romero, and M. H. Tonini, "Internal solitary waves from L-band SAR over the argentine inner patagonian shelf," *Remote Sens. Lett.*, vol. 11, no. 6, pp. 525–534, Mar. 2020, doi: 10.1080/2150704X.2020.1736725.

[10] N. J. Raju, M. K. Dash, S. P. Dey, and P. K. Bhaskaran, "Potential generation sites of internal solitary waves and their propagation characteristics in the andaman sea—A study based on MODIS true-colour and SAR observations," *Environ. Monitor. Assessment*, vol. 191, no. S3, pp. 809–819, Dec. 2019, doi: 10.1007/s10661-019-7705-8.

[11] W. Alpers and I. Hennings, "A theory of the imaging mechanism of underwater bottom topography by real and synthetic aperture radar," *J. Geophys. Res.*, vol. 89, no. C6, pp. 10529–10546, Nov. 1984, doi: 10.1029/JC089iC06p10529.

[12] W. Alpers, "Theory of radar imaging of internal waves," *Nature*, vol. 314, no. 6008, pp. 245–247, Mar. 1985, doi: 10.1038/314245a0.

[13] J.-S. Lee and E. Pottier, *Polarimetric Radar Imaging: From Basics to Applications*. Boca Raton, FL, USA: CRC Press, 2009, pp. 171–193.

[14] D. L. Schuler, R. W. Jansen, J. S. Lee, and D. Kasilingam, "Polarisation orientation angle measurements of ocean internal waves and current fronts using polarimetric SAR," *IEE Proc. Radar, Sonar Navigat.*, vol. 150, no. 3, pp. 135–143, Jun. 2003, doi: 10.1049/ip-rsn:20030492.

[15] L. J. Li, J. M. Meng, X. Zhang, and L. N. Sun, "Comparison for the visibility of the SAR polarization characteristics and images of internal waves," *J. Mar. Sci.*, vol. 32, no. 2, pp. 23–34, Jun. 2014, doi: 10.3969/j.issn.1001-909X.2014.02.003.

[16] J. C. Souyris and S. Mingot, "Polarimetry based on one transmitting and two receiving polarizations: The $\pi/4$ mode," in *Proc. IEEE Int. Geosci. Remote Sensing Symp.*, vol. 1, Jul. 2002, pp. 629–631, doi: 10.1109/IGARSS.2002.1025127.

[17] R. K. Raney, "Hybrid-polarity SAR architecture," *IEEE Trans. Geosci. Remote Sens.*, vol. 45, no. 11, pp. 3397–3404, Nov. 2007, doi: 10.1109/TGRS.2007.895883.

[18] R. Shirvany, M. Chabert, and J.-Y. Tourneret, "Ship and oil-spill detection using the degree of polarization in linear and Hybrid/Compact dual-pol SAR," *IEEE J. Sel. Topics Appl. Earth Observ. Remote Sens.*, vol. 5, no. 3, pp. 885–892, Jun. 2012, doi: 10.1109/JSTARS.2012.2182760.

[19] C. H. Cao, J. Zhang, J. M. Meng, X. Zhang, and X. P. Mao, "Analysis of ship detection performance with full-, compact-and dual-polarimetric SAR," *Remote Sens.*, vol. 11, no. 18, pp. 2160–2183, Sep. 2019, doi: 10.3390/rs11182160.

[20] A.-B. Salberg, O. Rudjord, and A. H. S. Solberg, "Oil spill detection in hybrid-polarimetric SAR images," *IEEE Trans. Geosci. Remote Sens.*, vol. 52, no. 10, pp. 6521–6533, Oct. 2014, doi: 10.1109/TGRS.2013.2297193.

[21] Y. Jiang, X. L. Zhang, and J. Shi, "Speckle reduction for polarimetric SAR images by improved Lee filter," *J. Univ. Electron. Sci. Technol. China*, vol. 38, no. 1, pp. 5–8, Jan. 2009, doi: 10.1016/j.apm.2007.10.019.

[22] H. Li, W. Perrie, Y. He, S. Lehner, and S. Brusch, "Target detection on the ocean with the relative phase of compact polarimetry SAR," *IEEE Trans. Geosci. Remote Sens.*, vol. 51, no. 6, pp. 3299–3305, Jun. 2013, doi: 10.1109/TGRS.2012.2224119.

[23] S. R. Cloude, D. G. Goodenough, and H. Chen, "Compact decomposition theory," *IEEE Geosci. Remote Sens. Lett.*, vol. 9, no. 1, pp. 28–32, Jan. 2012, doi: 10.1109/LGRS.2011.2158983.

[24] T. L. Ainsworth, S. R. Cloude, and J. S. Lee, "Eigenvector analysis of polarimetric SAR data," *IEEE Int. Geosci. Remote Sens. Symp.*, vol. 1, Feb. 2002, pp. 626–628, doi: 10.1109/IGARSS.2002.1025126.

[25] R. K. Raney, J. T. S. Cahill, G. W. Patterson, and D. B. J. Bussey, "The m-chi decomposition of hybrid dual-polarimetric radar data with application to lunar craters," *J. Geophys. Res.*, vol. 117, no. E12, pp. 5093–5096, May 2012, doi: 10.1029/2011JE003986.

[26] M. Dabboor, S. Howell, M. Shokr, and J. Yackel, "The Jeffries–Matusita distance for the case of complex Wishart distribution as a separability criterion for fully polarimetric SAR data," *Int. J. Remote Sens.*, vol. 35, no. 19, pp. 6859–6873, May 2014, doi: 10.1080/01431161.2014.960614.

[27] C. H. Cao, J. Zhang, X. Zhang, J. M. Meng, and J. Yue, "The analysis of ship target detection performance with C band compact polarimetric SAR," *Periodical Ocean Univ. China*, vol. 47, no. 2, pp. 85–93, Feb. 2017, doi: 10.16441/j.cnki.hdxb.20160347.

[28] J.-S. Lee, M. R. Grunes, T. L. Ainsworth, D. L. Schuler, and S. R. Cloude, "Unsupervised classification using polarimetric decomposition and the complex Wishart classifier," *IEEE Trans. Geosci Remote Sens.*, vol. 37, no. 5, pp. 2249–2259, Sep. 1999, doi: 10.1109/36.789621.

[29] S. Skrunes, C. Brekke, and T. Eltoft, "Characterization of marine surface slicks by Radarsat-2 multipolarization features," *IEEE Trans. Geosci. Remote Sens.*, vol. 52, no. 9, pp. 5302–5319, Sep. 2014, doi: 10.1109/TGRS.2013.2287916.

HAO ZHANG was born in Weifang, Shandong, China, in 1995. He received the B.S. degree in marine mapping from the Shandong University of Science and Technology, Qingdao, China, in 2014, and the M.S. degree from the First Institute of Oceanography, Ministry of Natural Resources of China, Qingdao, in 2020.

His research interests include detection of ocean internal waves using remote sensing images and characteristics of ocean internal waves.

JUNMIN MENG (Member, IEEE) received the B.S. degree in mathematics from Inner Mongolia Normal University, Urumqi, China, in 1996, the M.S. degree in applied mathematics from Inner Mongolia University, Urumqi, in 1999, and the Ph.D. degree in physical oceanography from the Ocean University of China, Qingdao, China, in 2002.

He is currently a Professor with the Laboratory of Marine Physics and Remote Sensing, First Institute of Oceanography, Ministry of Natural Resources, Qingdao. He is working on the development of algorithms determining marine parameters from microwave remote sensing.

LINA SUN was born in Huadian, Jilin, China, in 1985. She received the B.S. degree from Weifang University, Weifang, China, in 2005, and the M.S. degree from the Ocean University of China, Qingdao, China, in 2012.

Since 2012, she has been working as an Assistant Engineer with the First Institute of Oceanography, Ministry of Natural Resources, Qingdao, where she was an Engineer, in 2019. Her research interests include detection of ocean internal waves using remote sensing images and remote sensing data processing.

XI ZHANG (Member, IEEE) received the B.S. degree in information systems from the Qingdao University of Science and Technology, Qingdao, China, in 2005, and the M.S. degree in signal and information processing and the Ph.D. degree in computer science from the Ocean University of China, Qingdao, in 2008 and 2011, respectively.

He is currently an Associate Professor with the Laboratory of Marine Physics and Remote Sensing, First Institute of Oceanography, Ministry of Natural Resources, Qingdao. He has participated in several land-based and airborne geoscientific field studies, among which a number of campaigns were related to sea ice studies in the Bohai Sea. His research interests include microwave remote sensing of sea ice, numerical modeling of sea ice scattering, and synthetic aperture radar data analysis.

SIJING SHU was born in Huangshi, Hubei, China, in 1994. He received the M.S. degree from the First Institute of Oceanography, Ministry of Natural Resources of China, Qingdao, China, in 2020.

He is currently an Algorithm Engineer with PIESAT Information Technology Company Ltd., Beijing, China. His research interests include detection of marine oil spills using synthetic aperture radar and characteristics of films.